Quantitative phase imaging of weakly scattering objects using partially coherent illumination

Tan H. Nguyen,[1] Chris Edwards,[2] Lynford L. Goddard,[2] and Gabriel Popescu[1,*]

[1]*Quantitative Light Imaging Laboratory, Department of Electrical and Computer Engineering, Beckman Institute of Advanced Science and Technology, University of Illinois at Urbana-Champaign, Urbana, Illinois 61801, USA*
[2]*Micro and Nanotechnology Laboratory, Department of Electrical and Computer Engineering, University of Illinois at Urbana-Champaign, Urbana, Illinois 61801, USA*
[*]*gpopescu@illinois.edu*

Abstract: In this paper, we extend our recent work on partially coherent quantitative phase imaging (pcQPI) from two-dimensional (2D) to three-dimensional (3D) imaging of weakly scattering samples. Due to the mathematical complexity, most theoretical modeling of quantitative phase image formation under partial coherence has focused on thin, well-focused samples. It is unclear how these abberations are affected by defocusing. Also, as 3D QPI techniques continue to develop, a better model needs to be developed to understand and quantify these aberrations when imaging thicker samples. Here, using the first order Born's approximation, we derived a mathematical framework that provides an intuitive model of image formation under varying degrees of coherence. Our description provides a clear connection between the halo effect and phase underestimation, defocusing and the 3D structure of the sample under investigation. Our results agree very well with the experiments and show that the microscope objective defines the sectioning ability of the imaging system while the condenser lens is responsible for the halo effect.

OCIS codes: (030.1640) Coherence; (110.0180) Microscopy; (030.0030) Coherence and statistical optics; (100.5070) Phase retrieval.

References and links

1. G. Popescu, *Quantitative Phase Imaging of Cells and Tissues* (Mcgraw-Hill, 2011).
2. T. Ikeda, G. Popescu, R. R. Dasari, and M. S. Feld, "Hilbert phase microscopy for investigating fast dynamics in transparent systems," Opt. Lett. **30**(10), 1165–1167 (2005).
3. D. O. Hogenboom, C. A. Dimarzio, T. J. Gaudette, A. J. Devaney, and S. C. Lindberg, "Three-dimensional images generated by quadrature interferometry," Opt. Lett. **23**(10), 783–785 (1998).
4. D. Zicha and G. Dunn, "An image processing system for cell behaviour studies in subconfluent cultures," J. Microsc. **179**(1), 11–21 (1995).
5. M. Somekh, C. See, and J. Goh, "Wide field amplitude and phase confocal microscope with speckle illumination," Opt. Commun. **174**(1-4), 75–80 (2000).
6. Y. Park, C. A. Best, K. Badizadegan, R. R. Dasari, M. S. Feld, T. Kuriabova, M. L. Henle, A. J. Levine, and G. Popescu, "Measurement of red blood cell mechanics during morphological changes," Proc. Natl. Acad. Sci. U.S.A. **107**(15), 6731–6736 (2010).
7. Z. Monemhaghdoust, P. De Gol, F. Montfort, Y. Emery, C. Depeursinge, and C. Moser, "Towards an incoherent off-axis digital holographic microscope," in *SPIE BiOS* (International Society for Optics and Photonics2015), pp. 93360E–93360E–93365.
8. Z. Wang, L. Millet, M. Mir, H. Ding, S. Unarunotai, J. Rogers, M. U. Gillette, and G. Popescu, "Spatial light interference microscopy (SLIM)," Opt. Express **19**(2), 1016–1026 (2011).
9. B. Bhaduri, C. Edwards, H. Pham, R. J. Zhou, T. H. Nguyen, L. L. Goddard, and G. Popescu, "Diffraction phase microscopy: principles and applications in materials and life sciences," Adv. Opt. Photonics **6**(1), 57–119 (2014).
10. G. Popescu, L. P. Deflores, J. C. Vaughan, K. Badizadegan, H. Iwai, R. R. Dasari, and M. S. Feld, "Fourier phase microscopy for investigation of biological structures and dynamics," Opt. Lett. **29**(21), 2503–2505 (2004).
11. C. J. Sheppard and S. B. Mehta, "Phase microscope imaging in phase space," Proc. SPIE **9178A**, 97180 (2016).
12. S. Aknoun, P. Bon, J. Savatier, B. Wattellier, and S. Monneret, "Quantitative retardance imaging of biological samples using quadriwave lateral shearing interferometry," Opt. Express **23**(12), 16383–16406 (2015).
13. C. Zuo, Q. Chen, L. Tian, L. Waller, and A. Asundi, "Transport of intensity phase retrieval and computational imaging for partially coherent fields: The phase space perspective," Opt. Lasers Eng. **71**, 20–32 (2015).

#262749 Received 7 Apr 2016; revised 10 May 2016; accepted 11 May 2016; published 19 May 2016

14. L. Tian and L. Waller, "3D intensity and phase imaging from light field measurements in an LED array microscope," Optica **2**(2), 104–111 (2015).
15. J. C. Wyant, "The evolution of interferometry from metrology to biomedical applications," Proc. SPIE **9718**, 97180 (2016).
16. J. Martinez-Carranza, K. Falaggis, and T. Kozacki, "Enhanced lateral resolution for phase retrieval based on the transport of intensity equation with tilted illumination," Proc. SPIE **9718**, 97180 (2016).
17. S. Shin, Y. Kim, K. Lee, K. Kim, Y.-J. Kim, H. Park, and Y. Park, "Common-path diffraction optical tomography with a low-coherence illumination for reducing speckle noise," Proc. SPIE **9336**, 933629 (2015).
18. M. H. Jenkins and T. K. Gaylord, "Quantitative phase microscopy via optimized inversion of the phase optical transfer function," Appl. Opt. **54**(28), 8566–8579 (2015).
19. K. Lee, K. Kim, J. Jung, J. Heo, S. Cho, S. Lee, G. Chang, Y. Jo, H. Park, and Y. Park, "Quantitative phase imaging techniques for the study of cell pathophysiology: from principles to applications," Sensors (Basel) **13**(4), 4170–4191 (2013).
20. X. Ou, R. Horstmeyer, C. Yang, and G. Zheng, "Quantitative phase imaging via Fourier ptychographic microscopy," Opt. Lett. **38**(22), 4845–4848 (2013).
21. C. Zuo, Q. Chen, W. Qu, and A. Asundi, "Noninterferometric single-shot quantitative phase microscopy," Opt. Lett. **38**(18), 3538–3541 (2013).
22. A. El Mallahi, C. Minetti, and F. Dubois, "Automated three-dimensional detection and classification of living organisms using digital holographic microscopy with partial spatial coherent source: application to the monitoring of drinking water resources," Appl. Opt. **52**(1), A68–A80 (2013).
23. J. N. Clark, X. Huang, R. Harder, and I. K. Robinson, "High-resolution three-dimensional partially coherent diffraction imaging," Nat. Commun. **3**, 993 (2012).
24. S. Dong, R. Horstmeyer, R. Shiradkar, K. Guo, X. Ou, Z. Bian, H. Xin, and G. Zheng, "Aperture-scanning Fourier ptychography for 3D refocusing and super-resolution macroscopic imaging," Opt. Express **22**(11), 13586–13599 (2014).
25. B. Bhaduri, H. Pham, M. Mir, and G. Popescu, "Diffraction phase microscopy with white light," Opt. Lett. **37**(6), 1094–1096 (2012).
26. C. Edwards, B. Bhaduri, B. G. Griffin, L. L. Goddard, and G. Popescu, "Epi-illumination diffraction phase microscopy with white light," Opt. Lett. **39**(21), 6162–6165 (2014).
27. L. Mandel and E. Wolf, *Optical Coherence and Quantum Optics* (Cambridge University, 1995).
28. T. H. Nguyen, C. Edwards, L. L. Goddard, and G. Popescu, "Quantitative phase imaging with partially coherent illumination," Opt. Lett. **39**(19), 5511–5514 (2014).
29. C. Edwards, B. Bhaduri, T. Nguyen, B. G. Griffin, H. Pham, T. Kim, G. Popescu, and L. L. Goddard, "Effects of spatial coherence in diffraction phase microscopy," Opt. Express **22**(5), 5133–5146 (2014).
30. F. Zernike, "How I discovered phase contrast," Science **121**(3141), 345–349 (1955).
31. T. H. Nguyen, H. Majeed, C. A. Edwards, M. N. Do, L. L. Goddard, and G. Popescu, "Halo-free quantitative phase imaging with partially coherent light," Proc. SPIE **9336**, 93360 (2015).
32. Z. Yin, T. Kanade, and M. Chen, "Understanding the phase contrast optics to restore artifact-free microscopy images for segmentation," Med. Image Anal. **16**(5), 1047–1062 (2012).
33. T. Wilson and C. J. Sheppard, "The halo effect of image processing by spatial frequency filtering," Optik (Stuttg.) **59**, 19–23 (1981).
34. S. B. Mehta and C. J. Sheppard, "Using the phase-space imager to analyze partially coherent imaging systems: bright-field, phase contrast, differential interference contrast, differential phase contrast, and spiral phase contrast," ," J. Mod. Opt. **57**(9), 718–739 (2010).
35. J. Dohet-Eraly, C. Yourassowsky, A. El Mallahi, and F. Dubois, "Partial spatial coherence illumination in digital holographic microscopy: quantitative analysis of the resulting noise reduction," Proc. SPIE **9890**, 989004 (2016).
36. J. Dohet-Eraly, C. Yourassowsky, A. E. Mallahi, and F. Dubois, "Quantitative assessment of noise reduction with partial spatial coherence illumination in digital holographic microscopy," Opt. Lett. **41**(1), 111–114 (2016).
37. A. Kalyanov, N. Talaykova, and V. Ryabukho, "Formal theory of diffraction phase microscopy," Proc. SPIE **9448**, 944817 (2014).
38. J. C. Petruccelli, L. Tian, and G. Barbastathis, "The transport of intensity equation for optical path length recovery using partially coherent illumination," Opt. Express **21**(12), 14430–14441 (2013).
39. A. Ahmad, V. Dubey, G. Singh, V. Singh, and D. S. Mehta, "Quantitative phase imaging of biological cells using spatially low and temporally high coherent light source," Opt. Lett. **41**(7), 1554–1557 (2016).
40. Y. I. Nesterets and T. E. Gureyev, "Partially coherent contrast-transfer-function approximation," J. Opt. Soc. Am. A **33**(4), 464–474 (2016).
41. J. W. Goodman, *Statistical Optics* (John Wiley & Sons, 2015).
42. J. W. Goodman, *Statistical Optics* (Wiley-Interscience, 1985).
43. D. Gabor, "Microscopy by reconstructed wave-fronts," in *Proceedings of the Royal Society of London A: Mathematical, Physical and Engineering Sciences* (The Royal Society, 1949), pp. 454–487.
44. N. Streibl, "Three-dimensional imaging by a microscope," J. Opt. Soc. Am. A **2**(2), 121–127 (1985).

1. Introduction

Quantitative phase imaging (QPI) has developed into a key topic in the field of biomedical imaging as it offers intrinsic information on refractive index and sample topography (see [1] and the references therein). The quantity of interest in QPI is the optical path length variation

#262749 Received 7 Apr 2016; revised 10 May 2016; accepted 11 May 2016; published 19 May 2016

across the image field. This parameter is defined as the argument of a cross-correlation and thus, it can be extracted from interferometric experiments. The interferometric modalities can be divided into the *traditional* (e.g [2–7].) and *common-path* (e.g [8–24].) subgroups. The latter subgroup generates the reference field by spatially filtering the total field emerging from the sample. Hence, it possesses very high stability to ambient noise. A recent marriage between common path and white-light methods has further suppressed the speckle phenomenon, allowing highly sensitive measurements [8], [25], [26].An important benefit of these common path methods is the ability to be directly deployed from commercially available microscopes since only the total field relayed to the output port of the microscope is required. In QPI, the phase $\phi(\mathbf{r})$ is defined as (see Eq. (4).3-34 in [27]) the argument of the temporal cross-correlation function between the total field, $\mathbf{U}_t = \mathbf{U}_i + \mathbf{U}_s$ and a reference field $\mathbf{U}_r$, evaluated at zero delay, $\tau = 0$, [28] i.e. $\phi(\mathbf{r}) = \arg\left[J_{t,r}(\mathbf{r},\mathbf{r})\right]$, where $J_{t,r}(\mathbf{r},\mathbf{r}) = \Gamma_{t,r}(\mathbf{r},\mathbf{r},0) = \left\langle \mathbf{U}_t(\mathbf{r},t)\mathbf{U}_r^*(\mathbf{r},t)\right\rangle_t$. This quantity can be retrieved using any of aforementioned interferometric imaging modalities. Figure 1 shows the diffraction phase microscopy (DPM) setup [9] used in this paper. More information on how to obtain $J_{t,r}(\mathbf{r},\mathbf{r})$ from intensity measurements in DPM can be found in the Appendix A.

In recent publications [28, 29], we showed that, in common-path QPI modalities, the imperfection of the pinhole together with the partially coherent property of the illumination field may generate inaccuracy in the phase measurements. The net effect is an underestimation of the phase in regions of larger lateral extent than the coherence area and erroneous negative values at the edges. In phase contrast microscopy, this phenomenon is usually referred to as the halo effect [30]. A necessary condition for recording a halo free image without post-processing is the use of an illumination source with a coherence area that is larger than the field of view [29]. Otherwise, the data will be affected by the halo effect and phase underestimations. However, to our knowledge, most studies on these artifacts typically assumed thin, well-focused samples [31–40] where the sample is characterized by a transmission function $T(\mathbf{r}_\perp)$. To our knowledge, it is not yet clear how these effects vary when the sample is neither well-focused nor a good focus plane can be found. The later case usually happens when the thickness of the sample is not small enough compared to the depth of field. In this paper, we derive a model describing the image formation of common-path QPI under partially coherent illumination when the sample is characterized by its 3D susceptibility function $\mathrm{X}(\mathbf{r})$. The optical system scans axially (z-direction) through the volume of the object and phase measurements at multiple z-steps are recorded. Our derived model connects the phase measurement to the susceptibility of the sample. Also, similar to the 2D case, it explains the halo and phase-underestimation artifacts and provides a generalization to the 2D problem. We show that, under the Born settings, the measured phase is a high-pass version of an ideal phase, defined on the susceptibility of the sample. The high-pass filtering kernel describes the halo and phase-underestimation artifacts. More importantly, it only relates to the condenser of the imaging system and, invariant to defocusing. Therefore, the halo and phase-underestimation artifacts are unchanged due to defocusing. These effects can be seen from the data in Fig. 2 when scanning the sample over its z-stack over a range of [-20, 20] μm. Figures 2(a), 2(c) and 2(e) show 3D phase measurements for a transparent quartz micropillar 20 μm wide and 123 nm thick using the DPM setup shown in Fig. 1. The region under the influence of the halo does not seem to broaden or blur due to defocusing. Figures 2(e)-2(f) capture this observation by showing the x-z cross-sections over the entire z-range. Again, the sample gets blurred due to defocusing but the halo remains unaffected.

#262749 Received 7 Apr 2016; revised 10 May 2016; accepted 11 May 2016; published 19 May 2016

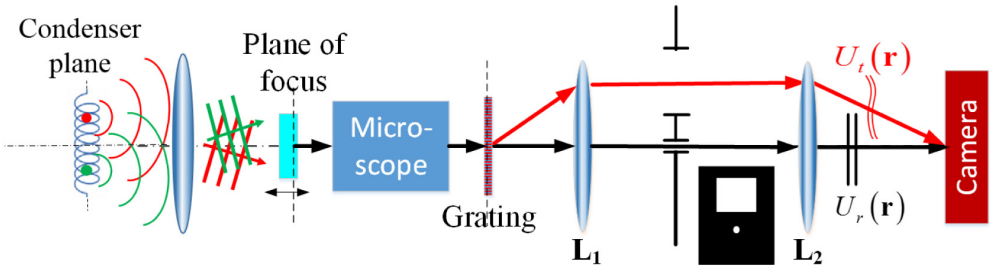

Fig. 1. A diffraction phase microscopy setup where two replicas of the total field at the output port of the microscope are generated by a diffraction grating. One of them is conjugated to the camera plane. The other is low-pass filtered by a physical pinhole to create a reference field. Interference fringes of these two fields are recorded by the camera and the measured phase of interest, $\phi(\mathbf{r})$, is obtained using the Hilbert transform. For more details, see [29].

2. Theory

Here, we propose a mathematical analysis that explains these phenomena for a 3D sample characterized by a refractive index function $n(\mathbf{r})$. We assume that the object is weakly scattering, so that the first-order Born approximation is applicable. Again, the reference field is generated by 2D spatially filtering the total field emanating from the sample, i.e. $\mathbf{U}_r(z) = \int \mathbf{U}_t(\mathbf{r}_\perp, z) d^2\mathbf{r}_\perp \equiv \mathbf{U}_{to}(z)$, where z is the axial coordinate. From now on, we will use the "o" subscript to denote the spatial filtering operation to generate the reference. The main result of our calculation is that the phase measured with partially coherent illumination, ϕ, is given by the following equation

$$\phi(\mathbf{r}) \approx \varphi(\mathbf{r}) - \varphi(\mathbf{r}) \circledv_{\mathbf{r}} h_i(\mathbf{r}) = \varphi(\mathbf{r}) \circledv_{\mathbf{r}} \left[\delta^{(3)}(\mathbf{r}) - h_i(\mathbf{r})\right]. \qquad (1)$$

where $\varphi(\mathbf{r})$ is the "ideal" phase, expected in conditions of perfect coherence, $h_i(\mathbf{r})$ is the spatial correlation function associated with the illuminating field, $\delta^{(3)}$ represents the 3D Dirac delta-function, and $\circledv_{\mathbf{r}}$ denotes the 3D convolution operation over the 3D coordinate $\mathbf{r}$. It can be seen from Eq. (1) that our measurement $\phi(\mathbf{r})$ is a high-pass filtered version of $\varphi(\mathbf{r})$ where the high-pass kernel is given by $\left[\delta^{(3)}(\mathbf{r}) - h_i(\mathbf{r})\right]$. More importantly, the kernel h_i, in spite of being a function of $\mathbf{r}$, only performs filtering in the transverse coordinate, $\mathbf{r}_\perp$, i.e. $h_i(\mathbf{r}) \propto \left[S(\mathbf{r}_\perp)/\tilde{S}(\mathbf{0})\right]\delta(z)$ (See the Appendix D for more details). Here, $S(\mathbf{r}_\perp)$ is the two-dimensional Fourier transform of the aperture intensity, also call the mutual intensity function of the illumination [41, 42], evaluated at the image plane. By the central ordinate theorem, we have $\tilde{S}(\mathbf{0}) \propto \int S(\mathbf{r}_\perp) d^2\mathbf{r}_\perp$, the spatial power spectrum of the illumination, evaluated at zero transverse spatial frequency, $\mathbf{k}_\perp = \mathbf{0}$. Consequently, the halo effect does not change over the axial dimension. Fully coherent illumination corresponds to a function h_i, that is uniform in x-y namely, $h_i(\mathbf{r}) = 1(\mathbf{r}_\perp)\delta(z)$. As a result, and $\phi(\mathbf{r}) \approx \varphi(\mathbf{r}) - const.$, which indicates that the measurement is ideal (up to an insignificant constant). The halo is absent in this case.

#262749 Received 7 Apr 2016; revised 10 May 2016; accepted 11 May 2016; published 19 May 2016

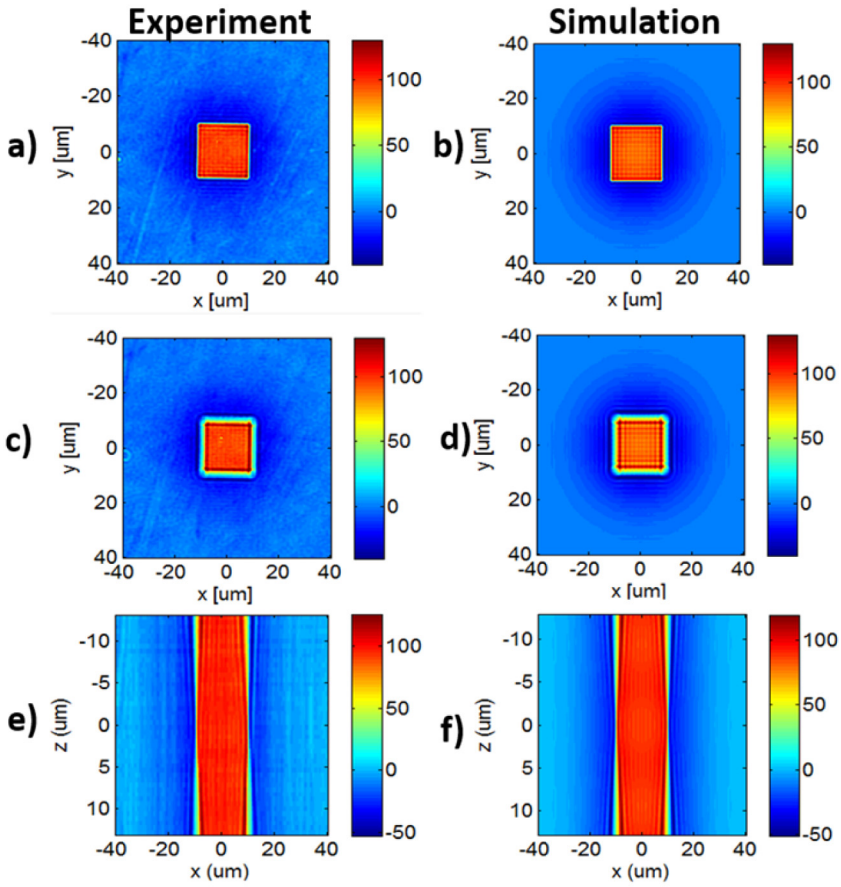

Fig. 2. Experimental (left) and simulated (right) thickness measurements in nanometers for 3D PC-QPI imaging of 20 μm width, 123 nm thick micropillars at $NA_c = 0.0072$. (a) and (b) show the thickness recovered from $\phi(\mathbf{r})$ at the sample plane. (c) and (d) are thickness measurements at +10 μm from the sample plane (forward scattering). (e), (f) show the xz cross-section for the thickness measurements at y = 0.0 μm. The halo and phase reduction can be seen for all these z-steps.

On the other hand, for incoherent illumination, i.e. $h_i(\mathbf{r}) = \delta^{(3)}(\mathbf{r})$, we have $\phi(\mathbf{r}) \to 0$, which establishes the impossibility of phase measurement under fully incoherent illumination. All intermediate cases between these two limits result in a phase image with low frequency attenuation in sharply transient areas, i.e., edges, lines, etc, while preserving high frequency information. This is the source of the halo effect commonly known in phase contrast microscopy [30]. More importantly, it can be seen that the kernel does not vary along the z-dimension and is not affected by defocusing. Equation (1) looks quite similar to its counterpart, Eq. (7) in [31]. However, there are fundamental differences between them. First, Eq. (1) tells that the measured phase, ϕ, is linearly related to the "ideal" phase, φ at each 3D coordinate $\mathbf{r}$. Meanwhile, Eq. (7) in [31], $\phi(\mathbf{r}_\perp) \approx \varphi(\mathbf{r}_\perp) - \left[e^{i\varphi} \circledv_{\mathbf{r}_\perp} h_i\right](\mathbf{r}_\perp)$, provides a non-linear relation between the measured phase, ϕ, and the "ideal" phase, φ, at each transverse coordinate $\mathbf{r}_\perp$. Second, the "ideal" phase in this paper is a function of the susceptibility which is a generalization of the "ideal" phase in [31], which is the argument of the sample transmission. We further show the convergence of this "ideal" phase to the argument of the sample transmission for thin sample in Appendix B.

#262749 Received 7 Apr 2016; revised 10 May 2016; accepted 11 May 2016; published 19 May 2016

Now, let us sketch out a proof for Eq. (1). For more details, please refer to the Appendix. We start by expressing the total and reference field as $\mathbf{U}_t = \mathbf{U}_i + \mathbf{U}_s$, and $\mathbf{U}_{to} = \mathbf{U}_{io} + \mathbf{U}_{so}$. Then, the cross-correlation function becomes

$$J_{t,r}(\mathbf{r},\mathbf{r}) = \left\langle \mathbf{U}_i + \mathbf{U}_s, \mathbf{U}_{io}^* + \mathbf{U}_{so}^* \right\rangle_t (\mathbf{r},\mathbf{r}) = J_{i,io}(\mathbf{r},\mathbf{r}) + J_{s,io}(\mathbf{r},\mathbf{r}) + J_{i,so}(\mathbf{r},\mathbf{r}) + J_{s,so}(\mathbf{r},\mathbf{r}), \tag{2}$$

where $J_{i,io}, J_{s,io}, J_{i,so}, J_{s,so}$ are cross-correlation functions, evaluated at zero-delay $\tau = 0$, between the incident field & its low-pass version, the scatter field & the incident low-pass version, the incident field & the scattering low-pass version, the scatter field & its low-pass version, respectively. Ignoring the $J_{s,so}(\mathbf{r},\mathbf{r})$ term due to its much smaller amplitude, the following results hold (see the Appendix C, D, E for short proofs).

$$J_{i,io}(\mathbf{r},\mathbf{r}) = \tilde{S}(\mathbf{0}), \tag{3}$$

$$J_{s,io}(\mathbf{r},\mathbf{r}) = i\tilde{S}(\mathbf{0})\varphi(\mathbf{r}), \tag{4}$$

$$J_{i,so}(\mathbf{r},\mathbf{r};0) = -i\tilde{S}(\mathbf{0})\left[\varphi(\mathbf{r}) \circledv_{\mathbf{r}} h_i(\mathbf{r})\right]. \tag{5}$$

Note that, among these terms, the first one, $J_{i,io}$, only relates to the illumination. The second and third terms are imaginary; they carry the sample information through the phase quantity $\varphi(\mathbf{r})$, which further relates to the susceptibility of the sample, $X(\mathbf{r})$. The fact that these two terms have opposite signs tells that they cancel out each other causing the phase-underestimation artifact. Using these terms, Eq. (1) can be proven easily using

$$\begin{aligned} \arg\left[J_{t,r}(\mathbf{r},\mathbf{r},0)\right] &= \arctan\left[\mathrm{Im}\left(J_{t,r}\right)/\mathrm{Re}\left(J_{t,r}\right)\right] \\ &= \arctan\left\{\left[J_{s,io}(\mathbf{r},\mathbf{r}) + J_{i,so}(\mathbf{r},\mathbf{r};0)\right]/J_{i,io}(\mathbf{r},\mathbf{r})\right\} \\ &= \varphi(\mathbf{r}) \circledv_{\mathbf{r}} \left[\delta^{(3)}(\mathbf{r}) - h_i(\mathbf{r})\right]. \end{aligned} \tag{6}$$

3. Experiments

To validate our model, we performed QPI measurements and simulations under various degrees of spatial coherence and defocusing. To change the coherence of the illumination, we vary the numerical aperture of the condenser NA_{con}. Smaller values of NA_{con} gives narrower spatial power spectrum of the illumination, $\tilde{S}(\mathbf{k}_\perp)$, and, hence, laterally broader h_i and vice versa. Four different values of NA_{con} were used: 0.0036, 0.0072, 0.014 and 0.09. We used quartz pillars as samples, the refractive index of which is 1.545 at the central wavelength 574 nm. The surrounding medium is air with refractive index of $\bar{n} = 1$. These parameters are used for simulation using Eq. (1). We obtained DPM measurements at several z-steps and with different values of the numerical aperture. The step size is set to 0.57 μm, which is about 4.6 times of the pillar's thickness. For each value of NA_{con}, z-steps in the range of [-12.5, 12.5] μm from the sample plane were acquired. Figures 2(b), 2(d), and 2(f) show our measurements and simulation results for the phase measurements at different z-positions for the case of NA_{con} = 0.0072. It can be seen that the simulation has an excellent agreement with the experiments shown in Figs. 2(a), 2(c), and 2(e). Figure 3 shows experimental and simulated cross-sectional profiles for the thickness measurements at different values of NA_{con} for the sample at two focal planes . The height profiles confirm the prior conclusion that, as the sample is scanned through focus, the object blurs but the halo remains constant. In our

#262749 Received 7 Apr 2016; revised 10 May 2016; accepted 11 May 2016; published 19 May 2016

simulation, we use a Gaussian profile for the spatial power spectrum, $\tilde{S}(\mathbf{k}_\perp)$, with standard deviation of $\overline{\beta} NA_{con}$. Good agreement between the simulated and measured profiles can be seen at the sample plane in Figs. 3(a) and 3(b). However, at 10 μm from the sample plane in Figs. 3(c) and 3(d), the simulation exhibits more significant modulation ("ringing") than the experimental results. This can be attributed to various smoothing effects in the optical setup and the fact that our simulation is based on monochromatic light, while in the actual experiment, the illumination has finite bandwidth around this frequency. Therefore, the diffraction ringing is washed out in experiments due to the combination of different diffraction kernels at different optical frequencies

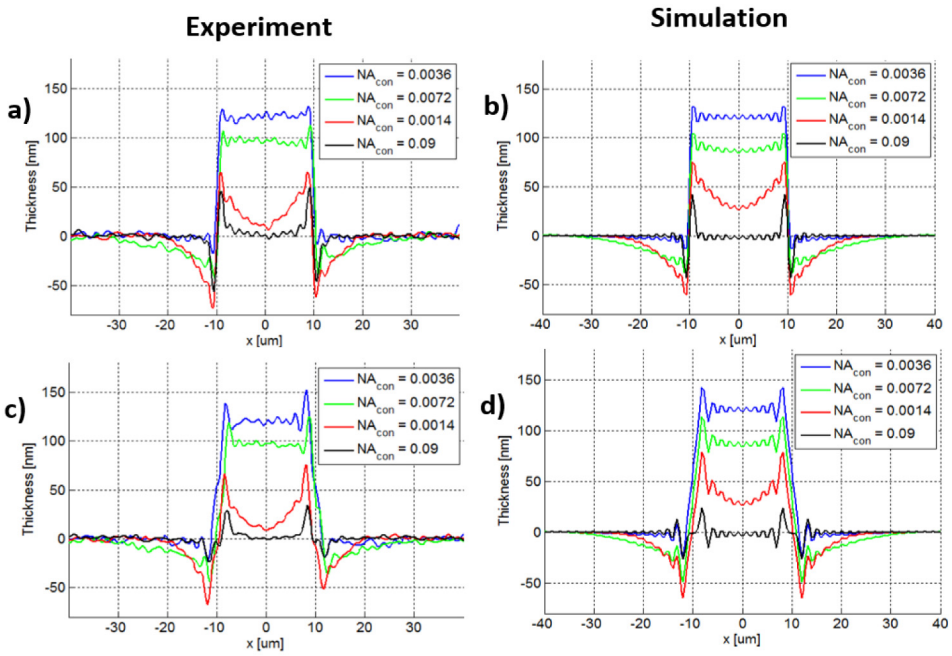

Fig. 3. Comparison between the experimental and simulated profiles for 123 nm quartz pillars for different values of NA_{con} at the plane of sample (a), (b) and at 10.0 μm from the plane of sample (c) and (d).

Figure 4 illustrates the independence of defocusing, which is due to the low-pass filtering performed by the microscope objective, as well as the halo effect, which is the results of low spatial coherence. Figure 4(a) shows three different x-z cross-sections of the phase measurement $\phi(x, y=0, z)$ for three different values of NA_{con}. The phase underestimation and halo effects can be seen in the second and the third cases. To get an insight of how these effects vary with respect to depth z, we take the 1D Fourier transform $\left|\tilde{\phi}(k_x, y=0, z)\right|$ of the cross-sections at z = 0.0 μm and z = 15.0 μm. We first find the regions in the spatial spectra that are affected by the halo only, defocusing only or both. From Eq. (1), it can be seen that the band-pass kernel $\left[\delta^{(3)}(\mathbf{r}) - h_i(\mathbf{r})\right]$ acts as a high-pass filter, suppressing low-frequency components of the ideal phase $\varphi(\mathbf{r})$. Hence, the spatial frequency domain can be divided into 2 regions. Region 1 is only affected by the defocusing and the frequency spectrum of the object $\tilde{\chi}$. Region 2 is affected by all contributions, including defocusing, low-frequency suppression and $\tilde{\chi}$. It is clear from Fig. 4(b) that for each z-position, the amplitude spectra in

#262749 Received 7 Apr 2016; revised 10 May 2016; accepted 11 May 2016; published 19 May 2016

region 1 are almost identical for each value of NA_{con}, indicating that the condenser aperture only affects the low-frequency range of the measured phase. Defocusing and depth sectioning only relate to the numerical aperture of the objective. Figures 4(c)-4(e) show amplitude spectra for the 3 different values of z at $NA_{con} = 0.0036, 0.0072,$ and 0.014 respectively. Note that the spectra are almost the same for region 2 for all 3 values of z, indicating that the low-frequency suppression due to the spatial coherence kernel $\left[\delta^{(3)}(\mathbf{r}) - h_i(\mathbf{r})\right]$ is essentially invariant to the depth z.

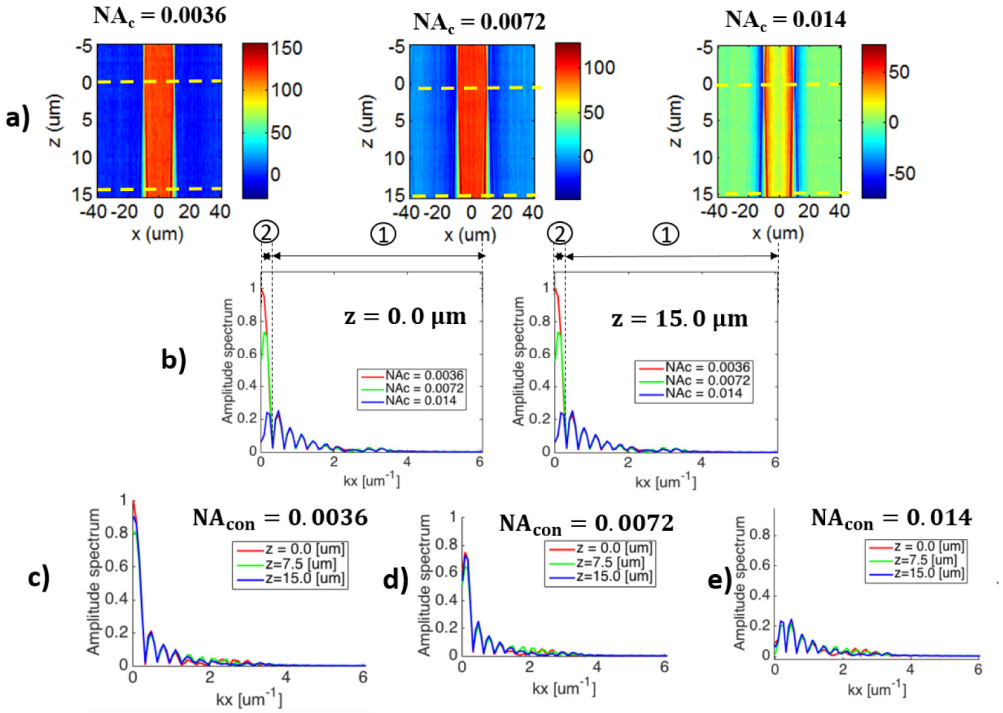

Fig. 4. (a) Three different x-z cross-sections of for 3 different values of the numerical apertures of the condenser. (b) Amplitude spectrum at z = 0.0 um and z = 15.0 um for tree values of NAcon. (c)-(e) Amplitude spectra for 3 different values of z at NAcon = 0.0036, 0.0072 and 0.014, respectively.

Next, we expand our analysis to thick, weakly scattering sample. Figure 5(a) shows x-y and x-z cross-sections of a simulated squared micropillar of dimension $30\times 30\times 25$ μm^3, . Here, the thickness is 25 μm. The pillar has refractive index of 1.01. The surrounding media has the refractive index of 1.00. Using the central wavelength of 0.574 μm, the total phase shift generated by this pillar is 2.19 rad. Here, we have intentionally chosen the thickness and the refractive index so that the total phase shift is less than 2π to avoid any possible phase wrapping. Figure 5(b) shows one x-z and three x-y cross-sections of the ideal phase, $\varphi(\mathbf{r})$, using its formula given in Eq. (9). The x-z one is evaluated through the center of the pillar at the plane $y = 0$ μm. The x-y ones are evaluated at three different planes $z = 0$, $z = -10$, $z = 20$ μm, denoted in the x-z cross-section. It can be seen that this the total phase shift of 2.19 rad can be observed in all three x-y cross-sections with different amount of defocusing. Figure 5(c) shows the x-z cross-sections of the measured phase under different numerical apertures of the condenser $NA_{con} = 0.0036, 0.0072,$ and 0.014 respectively. Dashed black rectangles denote the regions corresponding to the location of the pillar. Obviously, the halo and phase-under estimation get worse at larger values of the condenser aperture NA_{con}. These

#262749 Received 7 Apr 2016; revised 10 May 2016; accepted 11 May 2016; published 19 May 2016

effects are decoupled from the defocusing as discussed in the previous section. The code for our simulation can be obtained at https://github.com/thnguyn2/3D_halo_modeling.git.

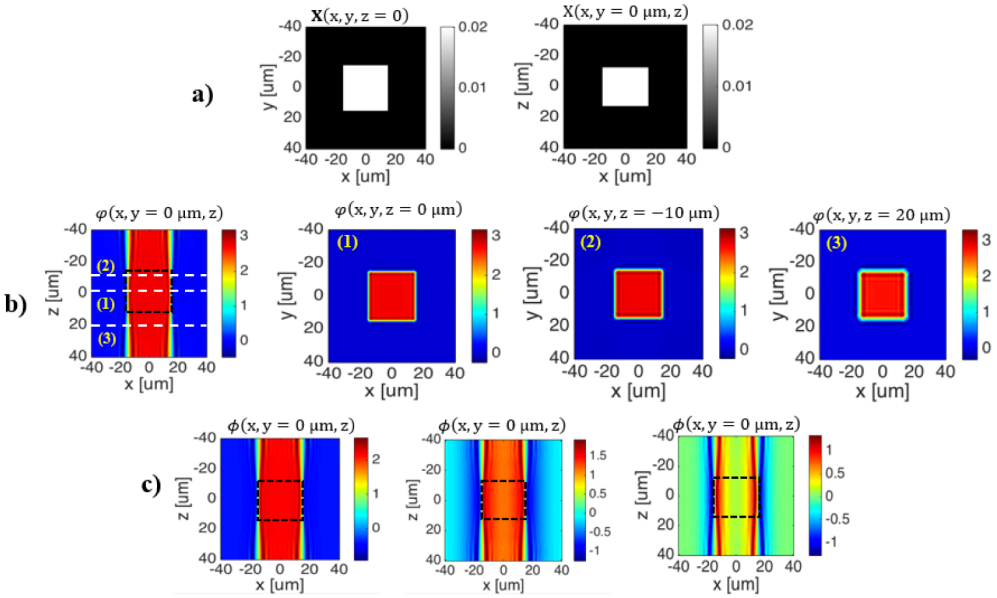

Fig. 5. (a) x-y and x-z cross-sections of a simulated micropillar of dimensions 30 x 30 x 25 μm3. (b) x-z and 3 x-y cross sections of the "ideal" phase, φ. The dashed rectangle denotes the locations of the micropillar. The next three cross-sections are evaluated at three different planes z = 0 μm, z = –10 μm, and z = 20 μm, denoted by while lines in the first x-z cross-section, respectively. (c) x-z cross-sections of the measured phase, ϕ, evaluated at three different values of NA_{con}, namely 0.0036, 0.0072 and 0.014.

5. Conclusion

In sum, we have developed a model to quantify the halo effect and phase reduction in 3D pcQPI experiments. Our model relates sample thickness, spatial coherence, defocusing, and field propagation to observed effects in the final measurement. The formalism is general and applicable to thin samples as well as thick, weakly scattering objects.

Appendix A: Extracting $J_{t,r}(\mathbf{r},\mathbf{r})$ from the interference fringes

The DPM intensity image captured by the camera can be written as $I(\mathbf{r}) = \left\langle \left| \mathbf{U}_r(\mathbf{r}) + \mathbf{U}_t(\mathbf{r}) \exp(ik_{xo}x) \right|^2 \right\rangle_t = I_r(\mathbf{r}) + I_t(\mathbf{r}) + J_{rt}(\mathbf{r},\mathbf{r}) \exp(-ik_{xo}x) + J_{tr}(\mathbf{r},\mathbf{r}) \exp(ik_{xo}x)$.

Here, k_{xo} is the spatial wave vector generated by the DPM grating. Note that the first two terms in the expansion of $J_{t,r}(\mathbf{r},\mathbf{r})$ exist at base-band while the third term and fourth term are centered around $\mathbf{k}_\perp = [\pm k_{xo}, 0]$ in the spatial frequency domain. Therefore, $J_{tr}(\mathbf{r},\mathbf{r})$ can be obtained by applying a band-pass filter on $I(\mathbf{r})$ so that its bandwidth matches to that of the fourth component, followed by shifting the remaining spectrum into baseband. This is the principle of off-axis holography proposed by Gabor [43].

#262749 Received 7 Apr 2016; revised 10 May 2016; accepted 11 May 2016; published 19 May 2016

Appendix B: The ideal phase $\varphi(\mathbf{r})$

The "ideal" phase is given as $\varphi(\mathbf{r}) = -\left[\overline{\beta}/(2\overline{n})\right]\left[X \circledv_{\mathbf{r}} \Im_{\mathbf{k}_\perp}^{-1}\left(e^{i(q-\overline{n}\overline{\beta})z}\right)\right](\mathbf{r})$. In order to show its connection with the sample transmission for thin sample in the two-dimensional case, let us consider a thin object, of thickness h, placed around the $z=0$ plane, characterized by the susceptibility function $\mathrm{X}(\mathbf{r}) = \Pi(z/h)\left[n(\mathbf{r}_\perp)^2 - \overline{n}^2\right] \approx 2\overline{n}\Pi(z/h)\left[n(\mathbf{r}_\perp) - \overline{n}\right]$, where $\Pi(.)$ is the rectangular function. We have also approximate $n(\mathbf{r}_\perp) + \overline{n} \approx 2\overline{n}$. For well-focus sample, ignore the defocusing diffraction i.e. $\Im_{\mathbf{k}_\perp}^{-1}\left(e^{i(q-\overline{n}\overline{\beta})z}\right) \to \delta^{(2)}(\mathbf{r}_\perp)1(z)$, we have $\varphi(\mathbf{r}) \to -h\overline{\beta}\left[n(\mathbf{r}_\perp) - \overline{n}\right]$, which is the definition of phase for the two-dimension case.

Appendix C: Proof of Eq. (3)

We have $J_{i,io}(\mathbf{r},\mathbf{r};0) = \left\langle \mathbf{U}_i(\mathbf{r}_\perp,z,t)\int \mathbf{U}_i^*(\mathbf{r}'_\perp,z,t)\,d^2\mathbf{r}'_\perp \right\rangle_t = \int J_{ii}(\mathbf{r}_\perp,z,\mathbf{r}'_\perp,z)d^2\mathbf{r}'_\perp$.

Combine this equation with Eq. (14) of [44], in which $J_{ii}(\mathbf{r}_\perp,z,\mathbf{r}'_\perp,z) = \int \tilde{S}(\mathbf{k}_\perp)\exp\left[i\mathbf{k}_\perp.(\mathbf{r}_\perp - \mathbf{r}'_\perp)\right]d^2\mathbf{k}_\perp$, we have: $J_{i,io}(\mathbf{r},\mathbf{r};0) = \int\int \tilde{S}(\mathbf{k}_\perp)\exp\left[i\mathbf{k}_\perp.(\mathbf{r}_\perp - \mathbf{r}'_\perp)\right]d^2\mathbf{k}_\perp d^2\mathbf{r}'_\perp = \tilde{S}(\mathbf{0}_\perp)\int \delta^{(2)}(\mathbf{k}_\perp)d^2\mathbf{k}_\perp = \tilde{S}(\mathbf{0})$, which completes the proof for Eq. (3).

Appendix D: Proof of Eq. (4)

The scattered field is given using the 1st-order Born approximation as $\mathbf{U}_s(\mathbf{r};t) \approx -\overline{\beta}^2\int X(\mathbf{r}')\mathbf{U}_i(\mathbf{r}',t)\,g(\mathbf{r}-\mathbf{r}')d^3\mathbf{r}'$, where $g(.)$ is the Green's function. For simplicity, we ignored dispersion of the sample, i.e. $X(\mathbf{r}) = n(\mathbf{r})^2 - \overline{n}^2$ is independent of wavelength. The second term reduces to

$$\begin{aligned} J_{s,io}(\mathbf{r},\mathbf{r}) &= \left\langle \mathbf{U}_s(\mathbf{r}_\perp,z,t)\int \mathbf{U}_i^*(\mathbf{r}''_\perp,z,t)\,d^2\mathbf{r}''_\perp \right\rangle_t \\ &= -\overline{\beta}^2\left\langle \int X(\mathbf{r}')\mathbf{U}_i(\mathbf{r}'_\perp,z',t)\,g(\mathbf{r}-\mathbf{r}')d^3\mathbf{r}'\int \mathbf{U}_i^*(\mathbf{r}''_\perp,z,t)\,d^2\mathbf{r}''_\perp \right\rangle_t \\ &= -\overline{\beta}^2\iint X(\mathbf{r}')J_{ii}(\mathbf{r}'_\perp,z',\mathbf{r}''_\perp,z)\,g(\mathbf{r}-\mathbf{r}')\,d^3\mathbf{r}'d^2\mathbf{r}''_\perp. \end{aligned} \quad (7)$$

Again, Eq. (14) of [44] gives $J_{ii}(\mathbf{r}'_\perp,z',\mathbf{r}''_\perp,z) = \int \tilde{S}(\mathbf{k}_\perp)\exp\left[i\mathbf{k}_\perp.(\mathbf{r}'_\perp - \mathbf{r}''_\perp) + iq(\mathbf{k}_\perp)(z'-z)\right]d^2\mathbf{k}_\perp$, which greatly simplifies Eq. (7) to

$$\begin{aligned} &J_{s,io}(\mathbf{r},\mathbf{r}) = -\overline{\beta}^2\iint X(\mathbf{r}')\int \tilde{S}(\mathbf{k}_\perp)\exp\left[i\mathbf{k}_\perp.(\mathbf{r}'_\perp - \mathbf{r}''_\perp) + iq(\mathbf{k}_\perp)(z'-z)\right]d^2\mathbf{k}_\perp g(\mathbf{r}-\mathbf{r}')\,d^3\mathbf{r}'d^2\mathbf{r}''_\perp \\ &= -\tilde{S}(\mathbf{0}_\perp)\overline{\beta}^2\int X(\mathbf{r}')\,g(\mathbf{r}-\mathbf{r}')\exp\left[-i\overline{n}\overline{\beta}(z-z')\right]d^3\mathbf{r}' = -\tilde{S}(\mathbf{0}_\perp)\overline{\beta}^2\left\{X \circledv_{\mathbf{r}}\left[g\exp\left(-i\overline{n}\overline{\beta}z\right)\right]\right\}(\mathbf{r}). \end{aligned} \quad (8)$$

Under paraxial approximation $g(\mathbf{r}) \approx i\,\Im_{\mathbf{k}_\perp}^{-1}\left(e^{iqz}\right)/2\overline{n}\overline{\beta}$, Eq. (8) reduces to: $J_{s,io}(\mathbf{r},\mathbf{r}) = -i\tilde{S}(\mathbf{0}_\perp)\left\{X \circledv_{\mathbf{r}}\left\{\left[\overline{\beta}/(2\overline{n})\right]\Im_{\mathbf{k}_\perp}^{-1}\left[e^{i(q-\overline{n}\overline{\beta})z}\right]\right\}\right\}(\mathbf{r}). = i\tilde{S}(\mathbf{0}_\perp)\varphi(\mathbf{r})$ where

#262749 Received 7 Apr 2016; revised 10 May 2016; accepted 11 May 2016; published 19 May 2016

$$\varphi(\mathbf{r}) = -\left[\overline{\beta}/(2\overline{n})\right]\left[X \circledv_{\mathbf{r}} \Im_{\mathbf{k}_\perp}^{-1}\left(e^{i(q-\overline{n}\overline{\beta})z}\right)\right](\mathbf{r}). \tag{9}$$

Appendix E: Proof of Eq. (5)

$$\begin{aligned} J_{i,so}(\mathbf{r},\mathbf{r}) &= \left\langle \mathbf{U}_i(\mathbf{r}_\perp,z,t)\int \mathbf{U}_s^*(\mathbf{r}'_\perp,z,t)\,d^2\mathbf{r}'_\perp \right\rangle_t \\ &= \iint -\overline{\beta}^2 X^*(\mathbf{r}'')\left\langle \mathbf{U}_i(\mathbf{r}_\perp,z,t)\,\mathbf{U}_i^*(\mathbf{r}''_\perp,z'',t)\right\rangle g^*(\mathbf{r}'-\mathbf{r}'')\,d^3\mathbf{r}''d^2\mathbf{r}'_\perp \\ &= \iint -\overline{\beta}^2 X^*(\mathbf{r}'')J_{ii}(\mathbf{r}_\perp,z,\mathbf{r}''_\perp,z'')\,g^*(\mathbf{r}'_\perp-\mathbf{r}''_\perp,z-z'')\,d^3\mathbf{r}''d^2\mathbf{r}'_\perp. \end{aligned} \tag{10}$$

Using Eq. (14) of [44] and dropping the conjugate notation on X since it is a real function as well as changing the order of integration, we have:

$$\begin{aligned} J_{i,so}(\mathbf{r},\mathbf{r}) &= \iint -\overline{\beta}^2 X(\mathbf{r}'')\left\{\int \tilde{S}(\mathbf{k}_\perp)\exp\left[i\mathbf{k}_\perp.(\mathbf{r}_\perp-\mathbf{r}''_\perp)+iq(\mathbf{k}_\perp)(z-z'')\right]d^2\mathbf{k}_\perp\right\} g^*(\mathbf{r}'_\perp-\mathbf{r}''_\perp,z-z'')\,d^3\mathbf{r}''d^2\mathbf{r}'_\perp \\ &= \int -\overline{\beta}^2 X(\mathbf{r}'')\left\{\int \tilde{S}(\mathbf{k}_\perp)\exp\left[i\mathbf{k}_\perp.(\mathbf{r}_\perp-\mathbf{r}''_\perp)+iq(\mathbf{k}_\perp)(z-z'')\right]d^2\mathbf{k}_\perp\right\}\left\{\int g^*(\mathbf{r}'_\perp-\mathbf{r}''_\perp,z-z'')\,d^2\mathbf{r}'_\perp\right\}d^3\mathbf{r}''. \end{aligned} \tag{11}$$

Under the paraxial approximation: $\int g^*(\mathbf{r}'_\perp-\mathbf{r}''_\perp,z-z'')\,d^2\mathbf{r}'_\perp \approx -i\,\Im_{\mathbf{k}_\perp}^{-1}\left[e^{-i\overline{n}\overline{\beta}(z-z'')}\right]/2\overline{n}\overline{\beta}$, Eq. (11) reduces to:

$$\begin{aligned} &J_{i,so}(\mathbf{r},\mathbf{r}) = i\int \overline{\beta}/(2\overline{n})\,X(\mathbf{r}'')\left\{\int \tilde{S}(\mathbf{k}_\perp)\exp\left[i\mathbf{k}_\perp.(\mathbf{r}_\perp-\mathbf{r}''_\perp)+i\left[q(\mathbf{k}_\perp)-\overline{n}\overline{\beta}\right](z-z'')\right]d^2\mathbf{k}_\perp\right\}d^3\mathbf{r}'' \\ &= i\int \overline{\beta}/(2\overline{n})\,X(\mathbf{r}'')\left[\Im_{\mathbf{k}_\perp}^{-1}\left(e^{i(q-\overline{n}\overline{\beta})(z-z'')}\right)\circledv_{\mathbf{r}_\perp} S\right](\mathbf{r}-\mathbf{r}'')d^3\mathbf{r}'' \\ &= i\left[\overline{\beta}/(2\overline{n})\right]\left\{X\circledv_{\mathbf{r}}\Im_{\mathbf{k}_\perp}^{-1}\left(e^{i(q-\overline{n}\overline{\beta})z}\right)\circledv_{\mathbf{r}}\left[S(\mathbf{r}_\perp)\delta(z)\right]\right\} \\ &= i\tilde{S}(\mathbf{0}_\perp)\left\{X\circledv_{\mathbf{r}}\left\{\left[\overline{\beta}/(2\overline{n})\right]\Im_{\mathbf{k}_\perp}^{-1}\left(e^{i(q-\overline{n}\overline{\beta})z}\right)\right\}\circledv_{\mathbf{r}}\left\{\left[S(\mathbf{r}_\perp)/\tilde{S}(\mathbf{0}_\perp)\right]\delta(z)\right\}\right\}(\mathbf{r}) \\ &= i\tilde{S}(\mathbf{0}_\perp)\left\{X\circledv_{\mathbf{r}}\left\{\left[\overline{\beta}/(2\overline{n})\right]\Im_{\mathbf{k}_\perp}^{-1}\left(e^{i(q-\overline{n}\overline{\beta})z}\right)\right\}\circledv_{\mathbf{r}}h_i\right\}(\mathbf{r}) = -i\tilde{S}(\mathbf{0}_\perp)\{\varphi\circledv_{\mathbf{r}}h_i\}(\mathbf{r}), \end{aligned} \tag{12}$$

where h_i was defined as $h_i(\mathbf{r}) = \left[S(\mathbf{r}_\perp)/\tilde{S}(\mathbf{0})\right]\delta(z)$ as introduced in the main text.

Acknowledgment

This work was supported by the National Science Foundation (NSF) (CBET-0939511 STC, IIP-1353368). For more information, visit http://light.ece.illinois.edu/.